Volume 7, Number 1 *January 2025*

Nanomaterials Science & Engineering

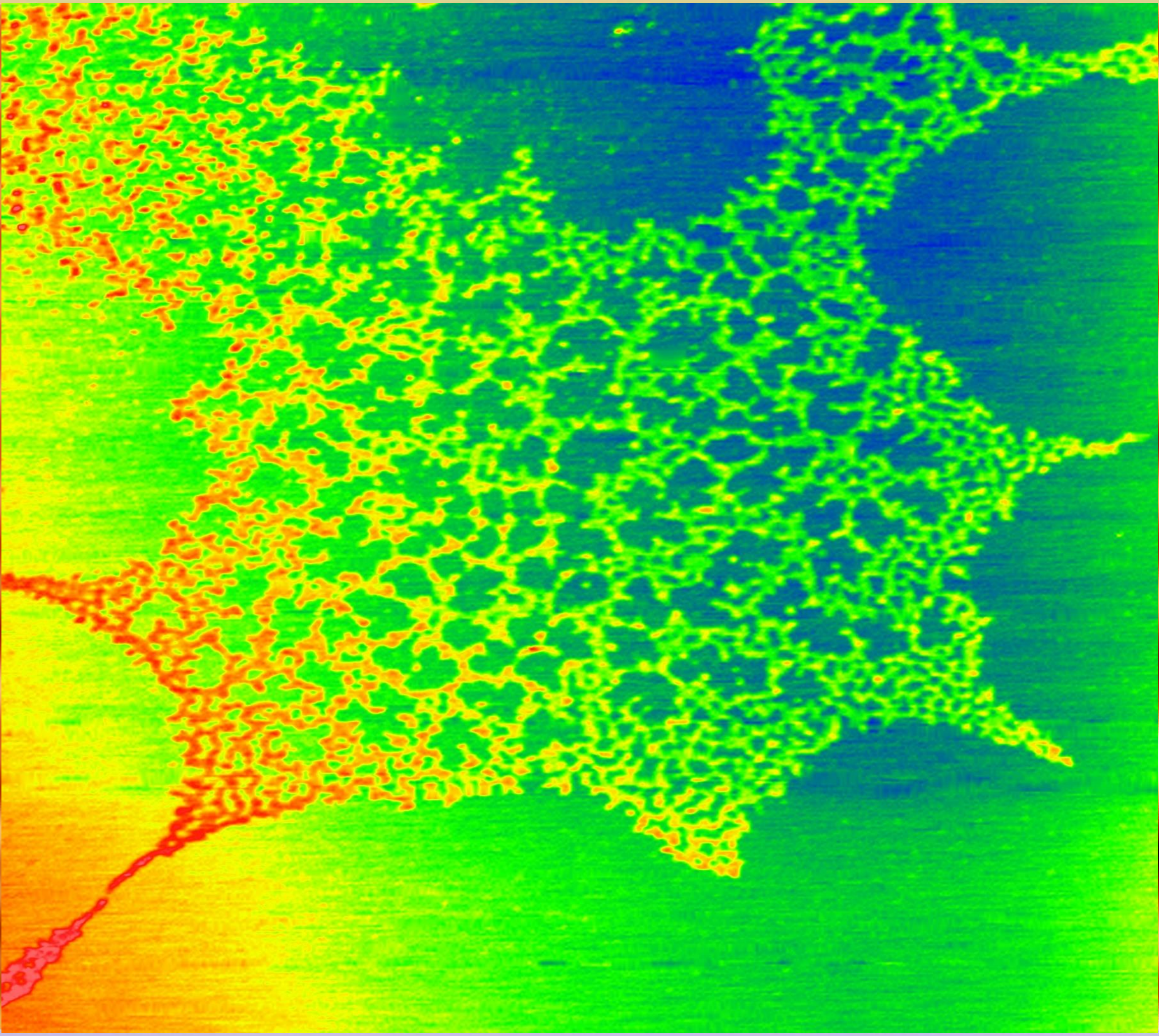

university of aveiro tema centre for mechanical technology and automation

Volume 7, Number 1 *January 2025*

Nanomaterials Science & Engineering

university of aveiro tema centre for mechanical technology and automation

Title
Nanomaterials Science & Engineering (NMS&E), Vol.7, No.1, 2025

Editors-in-Chief
Igor Bdikin
Paula Alexandrina de Aguiar Pereira Marques
Duncan Paul Fagg
Gil Gonçalves

Editorial Board
Alexander Titov, Andrei Kovalevsky, António Manuel de Amaral Monteiro Ramos, António Manuel de Bastos Pereira, António Manuel Godinho Completo, Bagautdinov Bagautdin, Binay Kumar, Budhendra Singh, Cicero R. Cena, D. Pukazhselvan, Dmitry A. Kiselev, Dmitry Karpinsky, Eudes Borges de Araujo, Gil Gonçalves, Gonzalo Guillermo Otero Irurueta, Indrani Coondoo, João Paulo Davim Tavares da Silva, José Coutinho, Maciej Wojtas, Manoj Kumar Singh, Margarida Isabel Cabrita Marques Coelho, Maxim Silibin, Münir Tasdemir, Neeraj Panwar, Nikolai Sobolev, Oleksandr Tkach, Paula Celeste da Silva Ferreira, Philip Leduc, Radheshyam Rai, Sergey Bozhko, Svitlana Kopyl, Vincent Ball, Vítor António Ferreira da Costa, Vladimir Bystrov, Yuri Dekhtyar

Editorial Managers
Igor Bdikin
Gil Gonçalves
Raul Simões

Cover Image
Gil Gonçalves (Carbon dots aggregates, Atomic Force Microscopy image, 3 μm x 3 μm)

Publisher
University of Aveiro

Support
Serviços de Biblioteca, Informação Documental e Museologia
Centre for Mechanical Technology & Automation (TEMA)
Mechanical Engineering Department
University of Aveiro

Copyright Information
All work licensed under Creative Commons Attribution License that allows others to share the work with an acknowledgement of the work's authorship and initial publication in this journal. Copyrights to illustrations published in the journal remain with their current copyright holders. It is the author's responsibility to obtain permission to quote from copyright sources.

Mailing Address
Department of Mechanical Engineering
University of Aveiro
Aveiro 3810-193
Portugal
E-mail: bdikin@ua.pt

ISSN: 2184-7002

Nanomaterials Science & Engineering (NMS&E), Vol.7, No.1, 2025

NANOMATERIALS
SCIENCE & ENGINEERING
Vol. 7, No. 1, pp. 5-13 (2025)

RESEARCH ARTICLE

https://doi.org/10.34624/nmse.v7i1.37480

An innovative approach to wound dressings: citric acid cross-linked carboxymethylcellulose-poly(vinyl alcohol) hydrogels with variable pore sizes

Yağmur CAMCI[1,2,*], Serbülent TÜRK[2,3], Mahmut ÖZACAR[2,4]

[1]*Sakarya University, Biomedical Engineering, Institute of Natural Sciences, Esentepe Campus, 54187, Sakarya, Turkey*
[2]*Biomaterials, Energy, Photocatalysis, Enzyme Technology, Nano & Advanced Materials, Additive Manufacturing, Environmental Applications and Sustainably Research & Development Group (BIOENAMS) R&D Group), 54187, Sakarya, Turkey*
[3]*BIMAS-RC, (Biomedical, Magnetic and Semiconductor Materials Application and Research Center), Sakarya University, 54187, Sakarya, Turkey*
[4]*Sakarya University, Science & Arts Faculty, Department of Chemistry, 54187, Sakarya, Turkey*
**Corresponding author, e-mail address: yagmur.camci@ogr.sakarya.edu.tr*

Received 14 August 2024; accepted 15 January 2025; published online 31 January 2025

ABSTRACT

Polyvinyl alcohol (PVA)/carboxymethyl cellulose (CMC) hydrogels were fabricated with varying concentrations of CMC. The hydrogels underwent cross-linking using non-toxic and biocompatible citric acid (CA) in combination with the freeze-thaw technique. FTIR analysis confirmed the hydrogels' chemical structures, while SEM characterization determined their pore diameters and porosity ratios. Hydrogels with diverse porosities exhibited suitable pore diameters for skin cells. Moreover, the hydrogels demonstrated a high swelling capacity, and the augmentation of CMC content resulted in increased water retention capacity. Their water vapor transmission, combined with their swelling properties, highlights their potential as suitable materials for use in wound dressings. These biopolymer-based hydrogels show promise for various applications, including wound dressings and biomimetic artificial skin, effectively replicating the properties of the epidermis and dermis.

1. INTRODUCTION

Skin constitutes ~20% of the body weight and is one of our largest organs [1]. Skin from the lower layer to the upper layers (from inside to outside) are listed as hypodermis (subcutaneous tissue), reticular dermis, papillary dermis, stratum basale, stratum spinosum, stratum granulosum, stratum lucidum, and stratum corneum. The predominant cell type of the epidermis is keratinocytes, which are also involved in forming the epidermal water barrier. Moreover, melanocytes manufacture the melanin pigment. Langerhans cells process antigens that enter the skin, and Merkel cells are concentrated in areas where sensory perception occurs immediately, such as the fingertips. In addition, the skin includes hair follicles and skin supplements like hair, sebaceous glands, and sweat glands [2].

The skin, which covers our body from the outside and protects us against physical damage from the environment, is injured throughout life for various reasons, such as injuries, surgery, and burns. These acute wounds heal in an acceptable period, and chronic wounds where healing takes longer and complete healing cannot occur.

Physiology of healing of skin injuries covers the stages of hemostasis, inflammation, proliferation, and remodeling [3]. Hemostasis is the body's first response to a wound to reduce blood loss by contracting blood vessels. During the inflammation stage, neutrophils migrate to the injured area and protect the wound against outside microorganisms. The proliferation stage includes granulation tissue beginning to form from the wound base and re-epithelialization [4]. During the remodeling stage, type 1 collagen is replaced by type 3 collagen, and the extracellular matrix is remodeled into a more mature structure with greater integrity [3]. These stages do not occur sequentially but rather in interlocking periods. In addition to traditional wound dressings used in wound healing, alginate dressings, polyurethane foam dressings, hydrogel dressings, hydrocolloid dressings, and nanofiber dressings are being developed to make wound healing more comfortable, support cell regeneration, and protect the wound against pathogens. Apart from wound dressings, artificial skin substitutes have also attracted attention in recent years. If we review these, Epidex, a permanent epidermal skin substitute, was commercially available in Switzerland in 2004 and produced for treating chronic wounds. *MySkin* was named biomedical product of the year in 2008 and is a permanent epidermal skin substitute used to treat chronic ulcers. *Suprathel* is a cell-free temporary epidermal skin substitute used in second and third-degree burn treatments. *Alloderm*, the most widely used brand of acellular dermal matrix, is a permanent dermal substitute. *Dermagraft* is a permanent dermal skin substitute derived from cryopreserved human fibroblast. *Biobrane* is a cell-free dermal skin substitute composed of nylon mesh and a thin layer of silicone, and more commercial products are available in addition to the products mentioned above.

Skin substitutes can be developed under in vitro, in vivo, and ex vivo conditions [5]. The most remarkable skin substitute production methods are the biopsy tissue method and the bioprinting method. In addition to the advantages of these methods, they also have disadvantages, such as ethical problems and difficulties in maintaining cell viability. Therefore, in this study, we focus on hydrogels that offer similar properties to skin. In the realm of literature, "hydrogel skin" encompasses hydrogels that exhibit both flexibility and electrical conductivity [6], [7], [8], in addition to those capable of facilitating drug release [9], [10] and possessing tissue adhesive [11], [12] properties intended for use on the skin.

In the study, we discussed poly(vinyl alcohol) (PVA) and carboxymethyl cellulose (CMC) based hydrogels, which are remarkable in many sectors such as biomedical, food packaging, and agricultural applications. CMC, a derivative of cellulose obtained from natural sources, is a biocompatible, water-soluble, non-toxic, and biodegradable biopolymer. The low strength problem of CMC can be overcome by using it together with PVA [13]. Citric acid (CA) is the cross-linking agent for PVA/CMC-based hydrogels. Classified as "generally recognized as safe" by the Food and Drug Administration [14], citric acid is an aliphatic organic acid known for its environmentally friendly, biodegradable properties. It can be quickly metabolized and eliminated from the body. Citric acid can create both physical and chemical cross-links. It forms cross-links with polymer chains via ionic interactions or hydrogen bonds at room temperature [15] esterifies the hydroxyl groups in nearby polymer chains to create cross-links at high temperatures [16].

2. MATERIALS AND METHODS

2.1. Materials

Polyvinyl alcohol (PVA, Mw: 60000) and citric acid monohydrate (CA, Mw: 210.14) were purchased from Merck, Germany. Carboxymethylcellulose sodium salt (CMC, Melting Point: >300 °C) was purchased from ThermoFisher, Germany. The entire chemicals were of analytical grade and were used as received without any purification.

2.2. Hydrogel Production for Lower Layer

10%wt. PVA solution and 1.66% wt. CMC solution was dissolved in distilled water in separate beakers in a magnetic stirrer. When the PVA solution became clear, the CMC solution was leisurely supplemented while continuing to stir. After mixing the mixture for a while, CA, 20% of the total polymer weight, was supplemented to the solution. The prepared hydrogel mixture was poured into Petri dishes and under room conditions for 1 night to remove air bubbles. Petri dishes containing a homogeneous hydrogel solution, free of air bubbles, were placed at -20 C for freezing. And 2 cycles of freeze-thaw were applied to the hydrogel (S1). The thawing process was carried out under room conditions.

Similarly, the weight ratio of the hydrogel, S2 polymers, which was later selected as the dermal skin substitute, was PVA: CMC 4:3. In the same way, CA was added 20% by weight of the total polymer, and the Petri dishes were under the room conditions for 1 night to remove air bubbles. After 2 cycles of freeze-thaw, the preparation of hydrogels was completed.

2.3. Hydrogel Production for the Upper Layer

Similar production steps were applied to the hydrogels prepared as dermal layer substitutes and to the hydrogels developed for the epidermal layer substitute. The aim of increasing the CMC and, therefore, the CA ratio in the hydrogel content is to aim for a smaller pore diameter and more cross-linking than the dermal substitute. This hydrogel (S3) was chosen as the epidermal skin substitute and had a PVA: CMC 1:1 weight ratio.

2.4. Characterization of PVA/CMC-Based Hydrogel

Fourier Transform Infrared (FTIR) spectra of lyophilized S1, S2, and S3 hydrogels and PVA, CMC, and CA dry powders were recorded with Spectrum Two FT-IR Spectrometer (PerkinElmer, USA). The samples were scanned in the wavenumber range of 400-4000cm^{-1} (20 scans with a resolution of 4 cm^{-1}).

2.5. Determination of Pore Size

All hydrogels were lyophilized and then cut, and the inner sides cut images of the hydrogels were perused under a field emission scanning electron microscope (FESEM, Quanta 450 FEG). 100x and 500x zoom FESEM images were examined with ImageJ software.

2.6. Swelling Study

The hydrogels were lyophilized and placed in 15 mL volume Falcon centrifuge tubes at room temperature, and the Falcon centrifuge tubes were filled with 10 mL distilled water. The initial weights (W_0) of the hydrogels were determined, and the weights of the hydrogels continued to be measured at regular intervals. The hydrogels' swelling ratios (%) in distilled water can be determined using the following equation:

$$SR\% = ((W_T - W_0)/W_0) \times 100\% \qquad (1)$$

W_0 is the initial weight of the hydrogels, while W_T is the weight of the hydrogels exposed to the application during time (t).

2.7. Water Retention Capacity of Hydrogels

Lyophilized hydrogels were swollen for 24 hours in Falcon centrifuge tubes filled with distilled water. The excess water (bulk water) on the surface of the hydrogel was eliminated with filter paper, and then the weight (W_W) of the hydrogel was determined. Hydrogels were placed in a hot air oven (37 °C) in open-top petri dishes. Water retention capacity (%) was calculated via Eq. (2):

$$\mathrm{W}RC\% = ((W_W - W_D)/W_W) \times 100\% \qquad (2)$$

W_W is the initial swollen (wet) weight of the hydrogels. W_D is the weight of hydrogels that lose water (dry) over time.

2.8. Determined of Water Vapor Transmission

Water vapor transmission of hydrogels (WVTH) characterization was performed under room conditions in a desiccator assembly. An open-mouth rectangular container (10.5 cm x 17 cm) was filled with 500 mL of water. The container filled with water was placed in the lower compartment of the desiccator. On top of the desiccator disc was a 50 mL falcon tube (ISOLAB, Turkey) filled with anhydrous calcium chloride. $CaCl_2$ was dried in the oven and weighed before being filled into the tube. The cap part of the $CaCl_2$-filled falcon tube was covered with hydrogel. There is no hygroscopic material other than $CaCl_2$ in the WVTH assembly. Finally, the $CaCl_2$ kept in the WVTH assembly for 1 night was weighed.

2.9. Gel Fraction Test

The lyophilized hydrogels were cut into square shapes (0.8 mm × 0.8 mm) and weighed 15±0.3 mg (W_0). For one day, hydrogels were swollen in 15 mL falcon tubes as in the swelling test. The excess water was removed from the surface of the hydrogel using filter paper and dried in an oven at 37±1°C for approximately 1 day until the weights of the hydrogels reached equilibrium and their weights were weighed (W_d).

The gel fraction (%) of hydrogels is determined using the following equation:

$$GF\ (\%) = ((W_0 - W_d)/W_0) \times 100\% \qquad (3)$$

W_0 is the initial weight of the hydrogels, while W_d is the reached equilibrium weight of the hydrogels.

3. RESULTS AND DISCUSSION

3.1. FTIR Analysis

A broad band of O-H stretching occurs at around 3400 cm^{-1}. The peak at 1086 cm^{-1} is characteristic for the C-O group of PVA [17]. The peak at 1586 cm^{-1} corresponds to the C=O stretching of the CMC carboxylate group. The band between wavelengths 1428 – 1282 cm^{-1} correlates with the CH groups' planar deformation. The band around 1057 cm^{-1} represents the C-O stretching of cellulose, hemicellulose, and aliphatic primary and

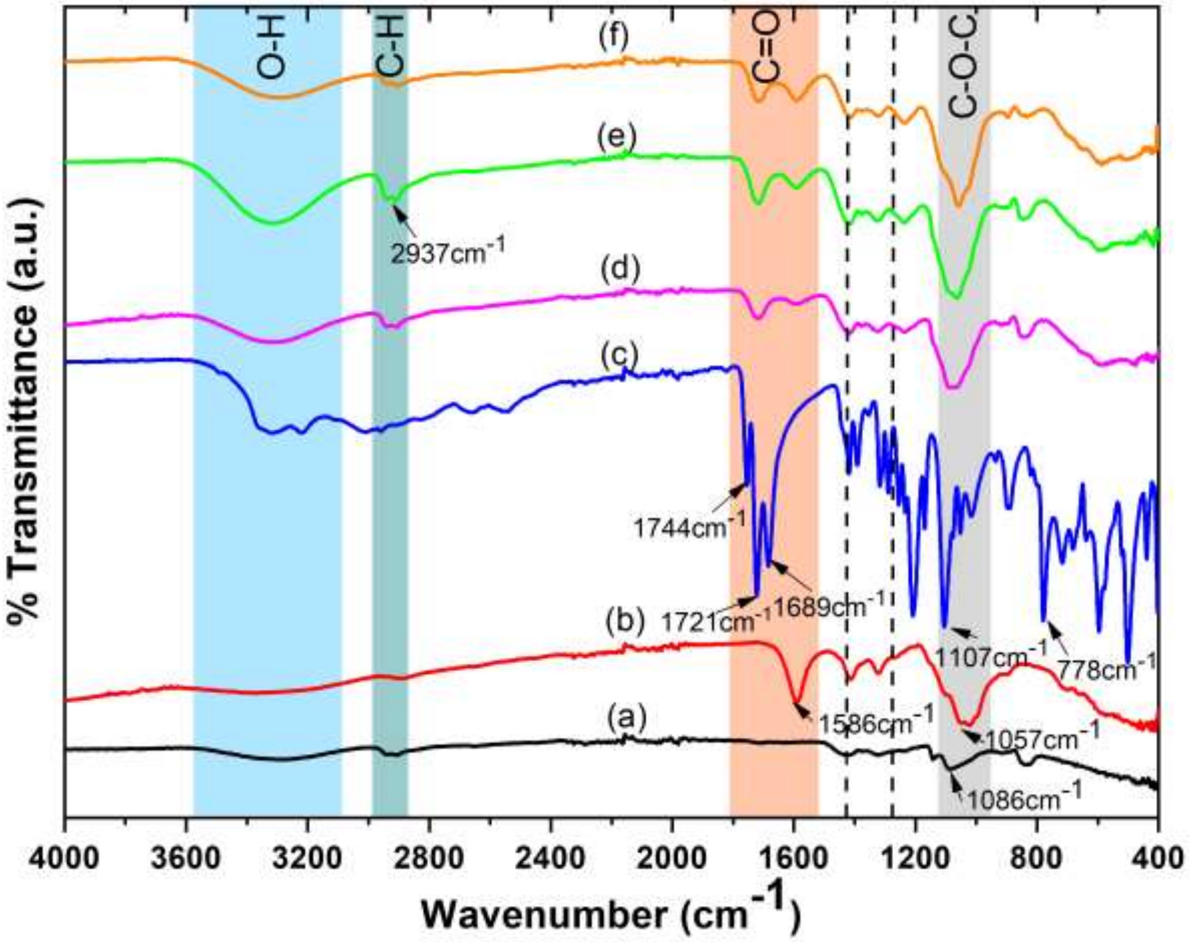

Figure 1. FT-IR spectra of (a) PVA powder, (b) CMC powder, (c) CA powder, (d) S1 hydrogel, (E) S2 hydrogel, (f) S3 hydrogel.

secondary alcohols. The peaks at 1744 cm^{-1}, 1721 cm^{-1}, and 1689 cm^{-1} refer to carboxylic acid and ester bonds [18]. Additionally, the peaks at 1107 cm^{-1} and 778 cm^{-1} are characteristic peaks of CA for C-O and C-C stretchings, respectively. The presence of a peak at 2937 cm^{-1}, corresponding to the saturated aliphatic C-H group in the cellulose chain, and the extension of the C-O-C band of the hydrogels to the 1078 cm^{-1} peak provides further evidence that CA participates in the structure as a cross-linker in the hydrogel matrix.

3.2. Study on the Pore Size of Hydrogels

Human skin cells have an average diameter of 40 μm [19]. The optimal pore size required for skin cell regeneration in adult mammals is 20-125 μm [20]. The predominant cell type of the epidermis is keratinocytes [21]. If the keratinocytes are less than 11 μm in diameter, it is able to proliferate (this can be up to 20 μm), but if the keratinocytes are larger than 20 μm in diameter, they cannot proliferate

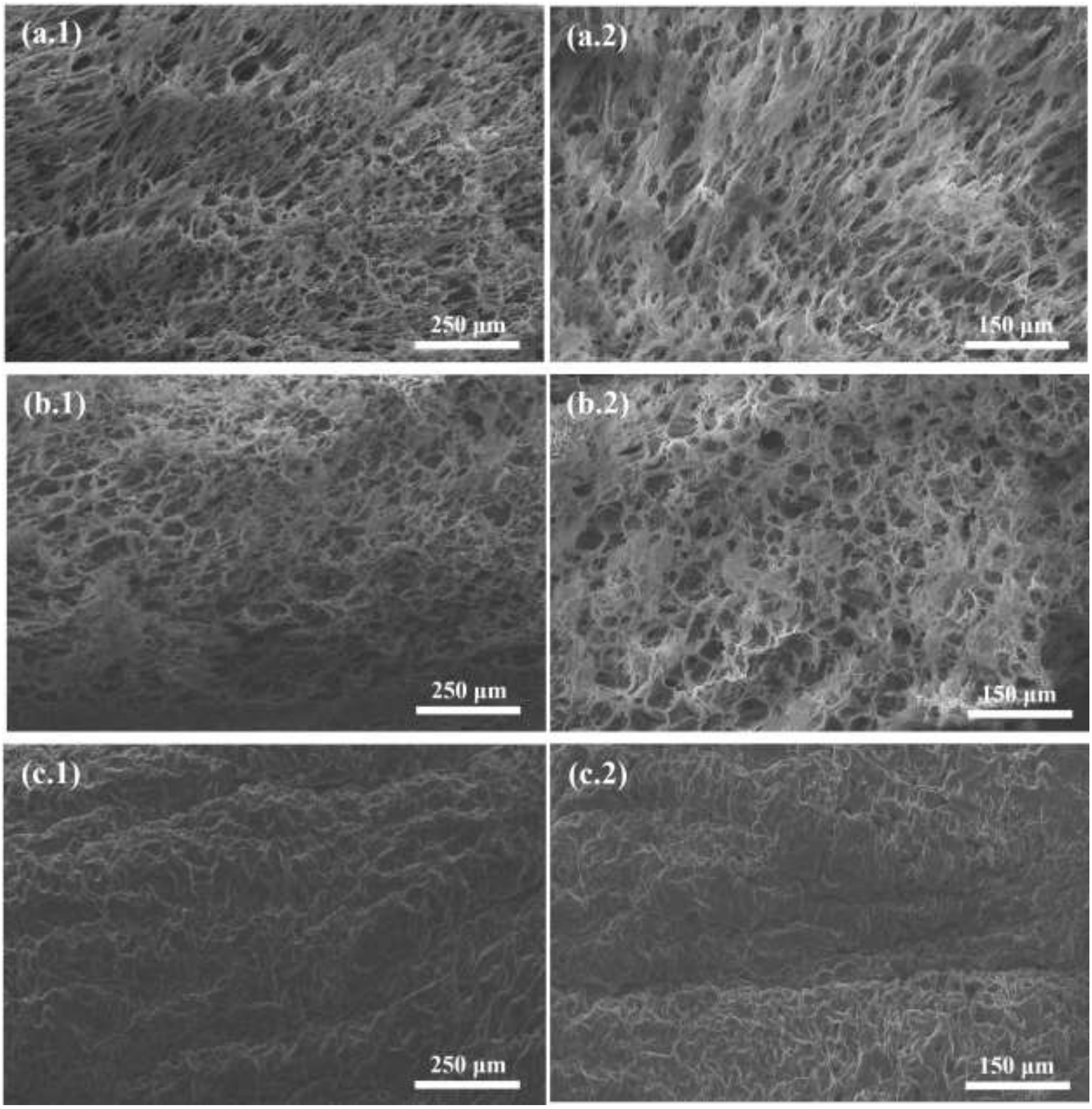

Figure 2. SEM images of hydrogels captured at various magnification levels are represented as follows: (a) S1, (b) S2, and (c) S3.

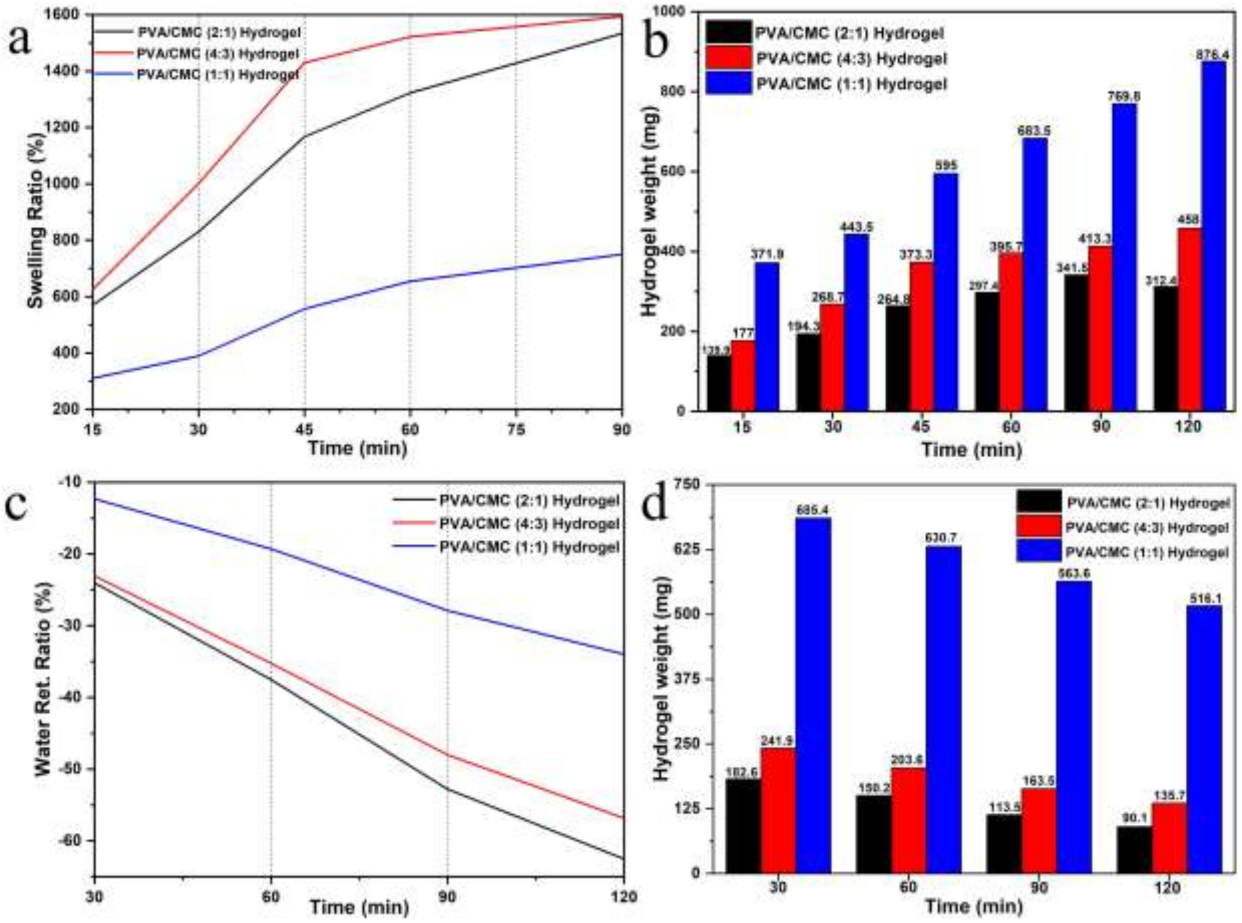

Figure 3. a) Swelling ratio (%) graph, b) Changes in the weight of hydrogels as they swell over time, c) Water retention capacity (%) graph, d) Water loss of hydrogels over time graph.

[22], they grow. Nonproliferating keratinocytes can grow up to 30 μm in diameter [23]. The papillary layer, located just below the epidermis, is rich in collagen (mainly type 1 collagen) and elastic fibrils [21]. Mizukoshi et al., as a result of their studies [24], [25], assumed that the dermal papillary structure' diameter was approximately 20 μm.

S1 has a porosity of 45.479% and pore sizes ranging from 2.714 to 69.158 μm. S2, chosen as the dermal layer substitute, has 63.722% porosity and pore sizes ranging from 2.244 to 73.539 μm. S3, selected as the epidermal skin substitute, has a porosity of 42.529% and pore sizes ranging from 3.429-32.620 μm. Hydrogel artificial skin substitutes with micropore sizes have a pore size appropriate for the regeneration of dermis and epidermis cells and a pore size sufficient for the growth of cells, as supported by the literature. While pores with an average diameter of 40 μm support new cell formation, pores <40 μm serve as cell scaffolds. Moreover, hydrogel artificial skin substitutes are in a range that will not prevent the adhesion of cells (cells cannot attach to >150μm pores [26], [27]). These results, obtained with FE-SEM images and ImageJ software, state that, as intended, the layers have different surface porosity ratios.

3.3. Swelling Analysis

When a dry hydrogel begins to swell in an aqueous environment, the most polar hydrophilic groups begin to hydrate first, called primary-bound water. As the polar groups hydrate and swell, the hydrophobic groups that interact with the remaining water molecules bind to the water, called secondary-bound water [28]. In the study, we noted that with the initial swelling of the hydrogels, their dry weight increased by 5.7 (S1), 6.25 (S2) and 3.1 (S3) times, respectively. The water capacity of the hydrogels reached equilibrium in approximately 90 minutes. The swelling analysis was continued throughout this period.

The results show that the swelling capacity of the hydrogel changes with the amount of CMC and the cross-linker effect, as reported by Bucak et al. (2022) [29]. Depending on the amount of CMC and total polymer in the hydrogels, the swelling capacity first increased with the increase in the amount of CA. Then, as our predictions and FESEM images show, the amount of water taken into the hydrogel matrix is restricted due to a tight network structure of S3.

3.4. Water Retention Analysis

The hydrogels were swollen for 24 h, and bulk water was removed from the hydrogels with filter paper. The water retention capacities of the hydrogels kept at 37 °C, representing the human body temperature, were determined with Equation 2. The hydrogels, which were measured 4 times, showed weight loss of 24.04%, 23.08%, and 12.31% of their W_W, respectively, in the first half hour. Conclusions show that S1 and S2 exhibited similar water retention capacity results, just like in the swelling analysis. Moreover, after two hours, the hydrogels lost 62.52%, 56.85%, and 34% of their weight. As supported by the literature [29], [30], we can also say that the hydrogel containing more CMC has a higher water retention capacity.

As explained in the introduction, keratinocytes are the dominant cells of the epidermis, and they participate in the epidermal water barrier. S3 provided the closest properties to the epidermal water barrier, having a higher water retention capacity and lower swelling capacity than other hydrogels. Another reason why we chose S3 as an epidermal skin substitute is its pore size (Fig. 2.). Although the hydrogels in our study do not fully provide the epidermal water barrier feature, increasing the amount of CMC shows that it will be effective in making the hydrogels similar to the epidermis layer.

3.5. Water Vapor Transmission

The air permeability of the hydrogel dressing was assessed by examining the water vapor permeability of S2, characterized by the highest pore volume and identified as the dermis equivalent with the highest gel fraction value. PVA/CMC-based hydrogels are designed as biomimic skin equivalents and wound dressings. Wound dressings should not completely deprive the wound of oxygen. They should allow gas inflow and outflow [31]. However, sudden discharge of water vapor dehydrates the wound and may cause the dressing to stick to the wound and cause secondary trauma.

The WVTH test was carried out using a desiccator setup. The water in the lower section of the desiccator evaporated and was retained by the hygroscopic $CaCl_2$ passing through the hydrogel membrane. The desiccator was sealed for one night, and the $CaCl_2$, initially with an oven-dried weight of 49.38 g, increased by 3.36% to reach 51.04 g.

The test, conducted under normal room conditions using a desiccator setup, confirmed that the hydrogel dressing allowed gas to enter the injured area.

3.5. Gelation Degrees of Hydrogels

Gel fraction analysis was performed to obtain information about the cross-linking capacity of hydrogel matrices. Gelling agents are divided into natural and synthetic group ensuring that the material becomes viscous or, in other words, thixotropic [32]. To determine the gelation degrees of PVA/CMC-based hydrogels, the lyophilized hydrogels were swollen and their weights were measured. Then, the hydrogels were dried until they reached their equilibrium weight, and their weights were measured again.

Cellulose derivatives are used as gelling agents. However, as mentioned in the literature [33], CMC-based hydrogels offer a gelation degree of approximately 40%. Similar to the literature, as a result of gel fraction analysis, the gelation degree of S1 (2:1) was measured as 38.73%, the gelation degree of S2 (4:3) as 48.61%, and the gelation degree of S3 (1:1) as 45.33%.

Compared to CMC-based hydrogels, recent hydrogel studies [34], [35] offer gelation degrees of >90%. In this context, the cross-linker ratio (CA ratio) is planned to increase the gelation degrees of CMC-based hydrogels in future studies.

4. CONCLUSIONS

PVA/CMC hydrogels were prepared at different ratios: S1 (2:1), S2 (4:3), and S3 (1:1). A non-toxic cross-linker, CA, was added at 20% by weight of the polymer, and the hydrogels were successfully produced using 2 cycles of the freeze-thaw process. The hydrogels exhibit a notable swelling capacity, which can swell up to 15 times their dry weight. An increased CMC ratio correlates with a higher water retention capacity in the swollen hydrogels. FESEM images analyzed with the ImageJ program show that the pore size of S1 ranges from 2.714 to 69.158 µm. S2 has a pore size ranging from 2.244 to 73.539 µm, and S3 exhibits pore sizes ranging from 3.429 to 32.620 µm. The hydrogels possess diverse pore sizes with suitable pore diameters that facilitate the proliferation and growth of skin cells while also functioning as a scaffold for skin cell growth. In addition to meeting the properties of biomimicry artificial skin, these hydrogels are also suitable for wound dressings; hydrogels have been proven to allow the exchange of gases. The results of the gel fraction of the hydrogels were found to be 43.67±4.94%. CMC-based hydrogels will be supported with different cross-linking techniques in future studies.

ACKNOWLEDGEMENTS

This work was supported by the Scientific Research Projects Commission of Sakarya University (Project Number: 2024-26-62-31).

REFERENCES

[1] M. Halem and C. Karimkhani, “Dermatology of the Head and Neck: Skin Cancer and Benign Skin Lesions,” *Dent Clin North Am*, vol. **56**, no. 4, pp. 771–790, Oct. 2012.

[2] D. H. Chu and C. A. Loomis, “Structure and Development of the Skin and Cutaneous Appendages,” *Fetal and Neonatal Physiology, 2-Volume Set*, pp. 490-498.e1, Jan. 2017.

[3] S. Singh, A. Young, and C. E. McNaught, “The physiology of wound healing,” *Surgery (Oxford)*, vol. **35**, no. 9, pp. 473–477, Sep. 2017.

[4] M. Alhajj, P. Bansal, and A. Goyal, “Physiology, Granulation Tissue,” *StatPearls*, Mar. 2020, Accessed: Dec. **21**, 2023.

[5] E. Sutterby, P. Thurgood, S. Baratchi, K. Khoshmanesh, and E. Pirogova, “Microfluidic Skin-on-a-Chip Models: Toward Biomimetic Artificial Skin,” *Small*, vol. **16**, no. 39, p. 2002515, Oct. 2020.

[6] R. Fu *et al.*, “A Tough and Self-Powered Hydrogel for Artificial Skin,” *Chemistry of Materials*, vol. **31**, no. 23, pp. 9850–9860, Dec. 2019.

[7] S. H. Kim *et al.*, “Ultrastretchable Conductor Fabricated on Skin-Like Hydrogel–Elastomer Hybrid Substrates for Skin Electronics,” *Advanced Materials*, vol. **30**, no. 26, p. 1800109, Jun. 2018.

[8] H. Yuk, T. Zhang, G. A. Parada, X. Liu, and X. Zhao, “Skin-inspired hydrogel–elastomer hybrids with robust interfaces and functional microstructures,” *Nature Communications 2016 7:1*, vol. **7**, no. 1, pp. 1–11, Jun. 2016.

[9] Y. Cai, L. Xin, H. Li, P. Sun, C. Liu, and L. Fang, “Mussel-inspired controllable drug release hydrogel for transdermal drug delivery: Hydrogen bond and ion-dipole interactions,” *Journal of Controlled Release*, vol. **365**, pp. 161–175, Jan. 2024.

[10] P. Dai *et al.*, “A Novel Methacryloyl Chitosan Hydrogel Microneedles Patch with Sustainable Drug Release Property for Effective Treatment of Psoriasis,” *Macromol Biosci*, vol. **23**, no. 12, p. 2300194, Dec. 2023.

[11] H. Jung *et al.*, “Adhesive Hydrogel Patch with Enhanced Strength and Adhesiveness to Skin for Transdermal Drug Delivery,” *Adv Funct Mater*, vol. **30**, no. 42, p. 2004407, Oct. 2020.

. Zeng, “Highly Adhesive Antibacterial Bioactive Composite Hydrogels With Controllable Flexibility and Swelling as Wound Dressing for Full-Thickness Skin Healing,” *Front Bioeng Biotechnol*, vol. **9**, p. 785302, Dec. 2021.

[13] V. Tyagi and A. Thakur, “Carboxymethyl cellulose-polyvinyl alcohol based materials: A review,” *Mater Today Proc*, Jan. 2023.

[14] R. Salihu *et al.*, “Citric acid: A green cross-linker of biomaterials for biomedical applications,” *Eur Polym J*, vol. **146**, Mar. 2021.

[15] P. Kaur *et al.*, “Waste to high-value products: The performance and potential of carboxymethylcellulose hydrogels via the circular economy,” *Cellulose*, vol. 30, no. 5, pp. 2713–2730, Mar. 2023.

[16] W. Zhang, S. Roy, E. Assadpour, X. Cong, and S. M. Jafari, “Cross-linked biopolymeric films by citric acid for food packaging and preservation,” *Adv Colloid Interface Sci*, vol. **314**, Apr. 2023.

[17] V. S. Ghorpade, R. J. Dias, K. K. Mali, and S. I. Mulla, “Citric acid crosslinked carboxymethylcellulose-polyvinyl alcohol hydrogel films for extended release of water soluble basic drugs,” *J Drug Deliv Sci Technol*, vol. **52**, pp. 421–430, Aug. 2019.

[18] F. Siregar, D. Nasution, Y. Muis, D.Y. Kaban, Preparation and characterization of antibacterial film based on carboxymethylcellulose from gebang leaf (Coryphautan), polyvinyl alcohol and citric acid, *Journal of Chemistry* **12** (2019) 554–564.

[19] M. M. Ismail, M. N. Shah Zainudin, R. A. Rahim, M. Alice, and N. Mohd Kassim, “An investigation of electromagnetic field effect on a human skin cell using numerical method approaches,” *IEEE International RF and Microwave Conference, RFM 2011 - Proceedings*, pp. 178–182, 2011.

[20] Z. Zhang, Y. Feng, L. Wang, D. Liu, C. Qin, and Y. Shi, “A review of preparation methods of porous skin tissue engineering scaffolds,” *Mater Today Commun*, vol. **32**, p. 104109, Aug. 2022.

[21] M. H. Ross, and W. Pawlina, Histology, p. 493-500, Lippincott Williams & Wilkins (2006).

[22] Y. Barrandon and H. Green, “Cell size as a determinant of the clone-forming ability of human keratinocytes.,” *Proceedings of the National Academy of Sciences*, vol. **82**, no. 16, pp. 5390–5394, Aug. 1985.

[23] T. T. Sun and H. Green, “Differentiation of the epidermal keratinocyte in cell culture: Formation of the cornified envelope,” *Cell*, vol. **9**, no. 4 PART 1, pp. 511–521, Dec. 1976.

[24] K. Mizukoshi, K. Yonekura, M. Futagawa, T. Nakamura, K. Hirayama, and K. Takahashi, “Changes in dermal papilla structures due to aging in the facial cheek region,” *Skin Research and Technology*, vol. **21**, no. 2, pp. 224–231, May 2015.

[25] K. Mizukoshi, T. Nakamura, and A. Oba, “The relationship between dermal papillary structure and skin surface properties, color, and elasticity,” *Skin Research and Technology*, vol. **22**, no. 3, pp. 295–304, Aug. 2016.

[26] B. K. H. L. Boekema *et al.*, “Effect of pore size and cross-linking of a novel collagen-elastin dermal substitute on wound healing,” *J Mater Sci Mater Med*, vol. **25**, no. 2, pp. 423–433, Feb. 2014.

[27] I. Bružauskaitė, D. Bironaitė, E. Bagdonas, and E. Bernotienė, “Scaffolds and cells for tissue regeneration: different scaffold pore sizes—different cell effects,” *Cytotechnology 2015 68:3*, vol. **68**, no. 3, pp. 355–369, Jun. 2015.

[28] I. Ćorković, A. Pichler, J. Šimunović, and M. Kopjar, “Hydrogels: Characteristics and Application as Delivery Systems of Phenolic and Aroma Compounds,” *Foods*, vol. **10**, no. 6, Jun. 2021.

[29] C. D. Bucak and M. O. Sahin, “Super-flexible, moldable, injectable, self-healing PVA/B/CMC hydrogels synthesis and characterization, as potential water-retaining agent in agriculture,” *Polymer Bulletin*, vol. **80**, no. 6, pp. 6591–6608, Jun. 2023.

[30] A. A. P. Mansur, M. A. Rodrigues, N. S. V. Capanema, S. M. Carvalho, D. A. Gomes, and H. S. Mansur, “Functionalized bioadhesion-enhanced carboxymethyl cellulose/polyvinyl alcohol hybrid hydrogels for chronic wound dressing applications,” *RSC Adv*, vol. **13**, no. 19, pp. 13156–13168, Apr. 2023.

[31] A. Sood, M. S. Granick, and N. L. Tomaselli, “Wound Dressings and Comparative Effectiveness Data,” *Adv Wound Care (New Rochelle)*, vol. **3**, no. 8, p. 511, Aug. 2014.

[32] Ajazuddin *et al.*, “Recent expansions in an emergent novel drug delivery technology: Emulgel,” *Journal of Controlled Release*, vol. **171**, no. 2, pp. 122–132, Oct. 2013.

[33] P. Liu, M. Zhai, J. Li, J. Peng, and J. Wu, “Radiation preparation and swelling behavior of sodium carboxymethyl cellulose hydrogels,” 2002.

[34] N. P. Esfahani, N. Koupaei, and H. Bahreini, “Fabrication and characterization of a novel hydrogel network composed of polyvinyl alcohol/polyvinylpyrrolidone/nano-rGO as wound dressing application,” *Journal of Polymer Research*, vol. **30**, no. 2, pp. 1–15, Feb. 2023.

[35] C. Greene, H. T. Beaman, D. Stinfort, M. Ramezani, and M. B. B. Monroe, “Antimicrobial PVA Hydrogels with Tunable Mechanical Properties and Antimicrobial Release Profiles,” *Journal of Functional Biomaterials* 2023, Vol. **14**, Page 234, Apr. 2023.

NANOMATERIALS
SCIENCE & ENGINEERING
Vol. 7, No. 1, pp. 14-19 (2025)

RESEARCH ARTICLE

https://doi.org/10.34624/nmse.v7i1.37198

Investigation of damping in porous metal foams

Bilal FETTAH [*], **Hamou ZAHLOUL**

Laboratory of Rheology and Mechanics, Hassiba Benbouali University of Chlef, Algeria
**Corresponding author, e-mail address: ba.fettah@univ-chlef.dz*

Received 30 July 2024; accepted 15 January 2025; published online 31 January 2025

ABSTRACT

Damping in materials and structure is known by the dissipation of energy over time under eventual action of an excitation called force. It is crucial characteristics in various engineering applications including civil engineering, mechanical engineering and aerospace engineering. It contributes to the safety, performances and longevity of these structures as well as the designed damping systems can improve the comfort and reliability of a wide range of engineering applications from everyday vehicles and machine to large scale engineering projects. The aim of this paper is to investigate damping mechanism in porous metal foams, the influence of different parameter such as porosity and microstructure on the damping phenomena and some practical implications. This research unlocks full potential of metal foams for vibration control and energy dissipation, advancing engineering solutions for a wide range of industries.

1. INTRODUCTION

In the past several decades, porous metal foams have played an important role in the development of various sectors. There are fast growing of its applications in medicine, mechanic, civil, marine and aerospace engineering. Foamed metals are porous materials which contains pores generally are open or closed. A common strategy used to manufacture metal foams is by preparing the blowing agent as a gas source to a molten metal then engineers add stabilized particles to the melt in order to obtain a uniform metal foam structure. Porous metal foams are lightweight material and typically retain some physical properties of their base metal. one of the major topics to be investigated in porous metal foams field is damping, it is crucial property in various applications.

Porous metal foams have excellent mechanical damping compared to the parent metal of which they are made [1]. Considering the internal damping is a form of dissipated energy within a material if it subjected to a cyclic stress, very limited knowledge is available about understanding mechanical damping and mechanisms of internal friction in porous metal foams [2]. At macroscopic approach, it is conventional that the dissipation of energy is the plasticity of a part of the system, high external forces generate important internal stresses that directly affect the mechanisms of generated damping. At microscopic level, we can distinguish damping in porous metal foams one by thermomechanical effects which considers damping in metals can be describe by the presence of thermal diffusion phenomena [3], the other by energy effects [4].

Although positive finding was presented in some research activities, predicting damping properties for porous metal foams in such application using finite element software is still missing.

However, damping determination of porous metal foams has rarely been analyzed. The only study on the damping properties of porous metal foams is that of [5] which they established first measurement related to damping loss factor in highly porous aluminum foam (up to 81.3%), they found that higher porosity produced higher loss factor damping. Banhart 1996 [6] enhances the finding of [5], they proposed a method to measure the loss factor of AlSi2 aluminum-silicon alloy foams of various densities with two types of special mount specimen. Beams as rectangular cross sections were normally used and driven into flexural vibrations, they concluded that damping is strongest in specimen with lowest apparent densities.

With the rapid growing of using porous metal foams in various applications, studying the damping and its structure dependence is a major concern. The way of producing open celled porous metal foams and the number of pores also effects on the damping and relative dynamic modulus behaviour [7].

Massimo Goletti et al [8] determined the damping parameters of aluminum foams beam by using two different test configurations based on vibrational method which they are modal shaker and instrumental hammer. They used the ASTM standard 2010 [9] to compute the loss factor for specific 3 eigenmode. They mainly found that the damping ratio is constant over frequency with the two different setups.

Furthermore, many studies have been carried out to investigate the effect of porous metal foams to eliminate the undesired vibrations of mechanical structures. Albertelli et al [10] proposed numerical simulation based on the finite element method to estimate damping in aluminum foamed filled tube in order to support the simple mechanical structures such as machine tools and its components.

Damping coefficient depends on the number of pores of porous metal foams. L.Dahil et al [11] investigated the effect of aluminum foams porosity on damping ratios by using experimental modal analysis method. It was observed from the frequency charts that the damping ratios increases with increasing the porosity.

In practical application, the demand for high strength with high damping of porous metal foams are necessarily required for ensuring good functionality and high safety. Many methods have been developed to improve damping properties in complicated structure for example in porous metal foams filled steel tube [12], it was found that under large vibration amplitude, the open pore aluminum foam and closed pore aluminum alloy can increase the level of mechanical damping more than five times than the steel tube itself.

Wang et al [13] improved the strength and enhance the damping properties of the nickel foam produced by chemical vapor deposition technique. They investigated the addition of graphene layer to the nickel foam ligaments in order to obtain both high strength and damping properties.

For this study, it was of interest to investigate damping in porous metal foams because it is an important area of research with implication for various engineering applications. Also, to develop a comprehensive understanding of the damping behaviour in porous metal foams by investigating the damping mechanisms at multiple scales. This research presents some practical advantages for readers to understand the phenomenon of damping in porous metal foams.

2. DAMPING MECHANISMS IN POROUS METAL FOAMS

Porous metal foams become well known material among researchers, they offer multiple potential for lightweight structures, energy absorption and for thermal management. Generally damping in materials and structure is very important to restrict mechanical vibrations and establish security and comfort. Previous studies have emphasized that Nickel Inconel superalloy and copper foams have shown promise for noise control and vibration suppression due to their unique mechanical properties [1]. These foams have high stiffness, excellent energy absorption, and good vibroacoustic damping. Despite their potential, porous metal foams are not widely used, but research and advancements in manufacturing processes are expected to increase their accessibility in the future [14]. Current methods, such as experimental modal analysis and finite element simulations, only provide valid results for specific structures and cannot predict damping behavior in new systems. To address this limitation, predictive models for damping properties have been developed. These models involve experimental tests and simulations on simple structures to define critical damping values. Based on these results, predictive models of damping factors can be established and validated on different structures.

Damping refers to the ability of a material to dissipate energy from mechanical vibrations. In the case of porous metal foams, their low density compared to traditional metals allows for promising damping capabilities relative to weight. Various mechanisms contribute to the damping behavior of cellular metallic materials. Many internal friction mechanisms that are present in dense metals also contribute to the damping in porous metal foams. The density of these foams can be as low as 1/10th or even lower than that of the metals used for their carcass [1]. This low density contributes to their potential for efficient energy dissipation.

There are several ways to characterize material damping. The loss coefficient η will be used to define the terms of energy dissipation. If a material is loaded elastically to a stress $\boldsymbol{\sigma_{max}}$ (see fig 1) it stores elastic strain energy per unit volume, U; in a complete loading cycle it dissipates ΔU, shaded in the fig 1, where:

$$U = \int_0^{\sigma_{max}} \sigma d\varepsilon = \frac{1}{2}\frac{\sigma_{max}^2}{E} \ \ and \ \ \Delta U = \oint \sigma d\varepsilon$$

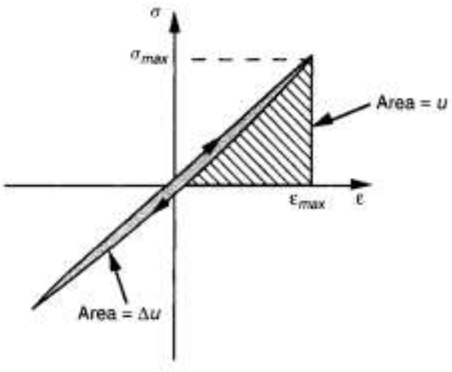

Figure 1. loss coefficient η measures the fractional energy dissipated in a stress-strain cycle [1]

The loss coefficient η is the energy loss per radian divided by the maximum elastic strain energy (or the total vibrational energy)

$$\eta = \frac{\Delta U}{2\pi U}$$

In general, the value of η depends on:

- frequency of cycling.
- temperature.
- amplitude of the applied stress or strain.

Other measures of damping include:

The proportional energy loss per cycle.
The damping ratio ξ.[15]
The logarithmic decrement δ.[16]
The loss angle ψ.
The quality factor Q.

Damping mechanisms in metal foams can be enhanced. With direct growth of graphene on the metal surfaces opens a door for high performance composites in a simple manner. Wang et al [13] investigated damping characteristics and mechanical strength of nickel foams by placed a graphene layer on the top surface of the porous foams specifically on the cell walls.

3. EFFECT OF POROSITY ON DAMPING

Porous metal foams have been found to possess high damping capabilities, with internal friction increasing as porosity increases and pore size decreases. This damping behaviour is independent of frequency and primarily depends on strain amplitudes. Metal foams with porosity values over 50% are particularly effective at attenuating vibrations, making them of interest to designers. In addition to their damping properties, metal foams also offer advantages such as a low weight-to-

Figure 2. Aluminum foam of 86% porosity.

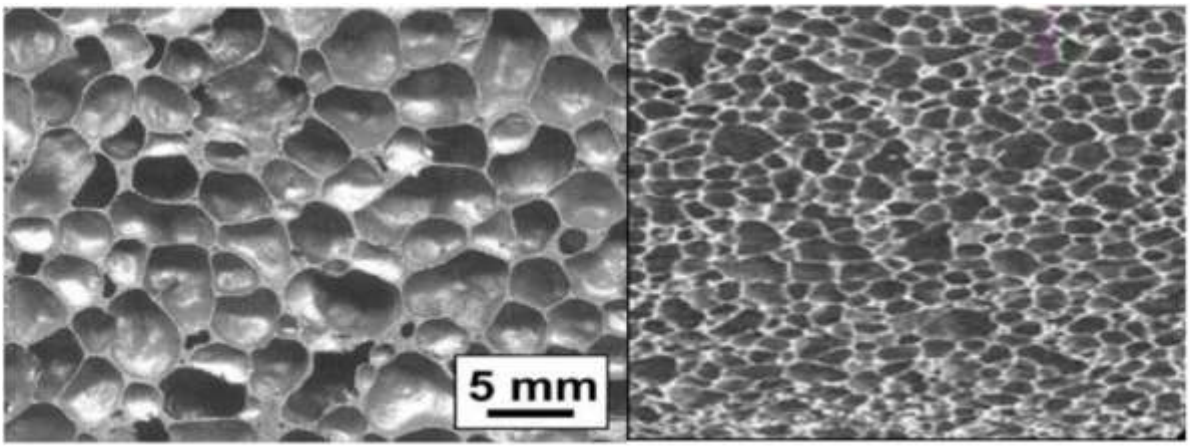

Figure 3. Closed cell aluminum foams [18]

stiffness ratio and high energy dissipation capacity, making them attractive for various industries [17].

3.1. Type of Porous Metal Foams

Metal foams can be divided into two types according to [18].

3.1.1. Closed Cell Metal Foams

The closed cell metal foams group (see fig 3) are appropriate for structural applications, such as energy absorbers or load bearing components, where light solutions are often built on stiffness/weight ratios that are as high as possible.

3.1.2. Open Cell Metal Foams

The open metal foams group (see fig 4) are mostly used in functional applications such as heat exchangers, filters, silencers, and catalyst support, where a liquid or gas must pass through the foam's degree of porosity.

Metal foams have been proposed for damping and anti-crash applications due to their energy-absorption properties. The damping properties of foam-filled tubes improve with the number of cycles, making them suitable for applications where damping is crucial. Open-cell nickel foams, in particular, are widely used in battery electrodes and exhibit unique features such as permeability, high tortuosity, and excellent electrical and thermal conductivity. Despite their desirable properties, the fabrication of metal foams still faces challenges due to the coexistence of solid, liquid, and gaseous phases at different temperatures. However,

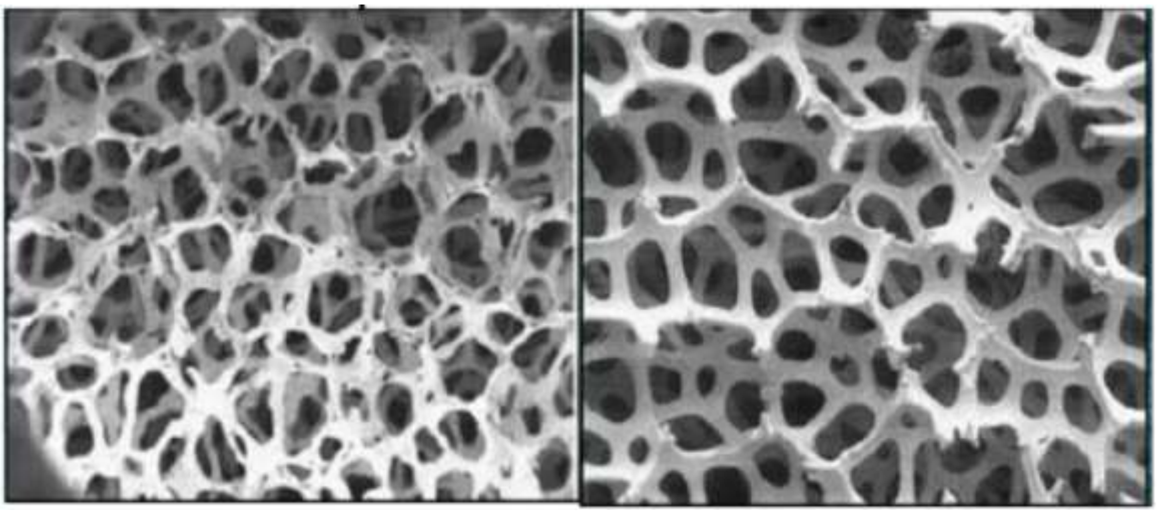

Figure 4. Open cell aluminum foams [18].

extensive research has provided valuable insights into the damping mechanisms and properties of porous metal foams. The damping behaviour of porous metal foams materials is influenced by various mechanisms of internal losses, such as thermoelastic and microeddy currents, magnetic domains, dislocations, and microcracks.

Porosity and specific foam structures are important factors that affect the damping characteristics of porous metal foams. Higher porosities often lead to better damping performance due to increased internal friction and energy dissipation.

4. FUTURE APPLICATION OF POROUS METAL FOAMS

The main applications of porous metal foams can be grouped into structural and functional and are based on several excellent properties of the material [18]. Structural applications take advantage of the lightweight and specific mechanical properties of metal foams; functional applications are based on a special functionality, i.e., a large open area in combination with very good thermal or electrical conductivity for heat dissipation or as electrode for batteries, respectively. We will review the applications of closed, partially open and open cell metal foams.in this section of the paper we will cite multiple application where foams are actively utilized.

4.1. Structural Application of metal foams

- Automotive industry [19]
- Energy absorption [20]
- Lightweight construction [2]
- Noise/sound absorption [19]
- Aerospace industry [21]
- Ship building [14]
- Railway industry [14]
- Machine construction [22]
- Biomedical industry

4.2. Functional Application of metal foams

- Filtration and separation
- Heat dissipation and cooling elements
- Support for catalysts
- Thermal storage energy application [23]
- Silencers [1]
- Fluid flow control
- Battery Electrodes [2]
- Spargers [1]
- Water decontamination and Acoustic control.

The open literature shows that porous metal foams are one of the most promising materials for fulfilling the increasing demands where certain properties such as acoustic, damping and thermal characteristics are required. However, metal foams have limited noise absorption capability but still enough to be useful for various multifunctional applications in different sectors.

To note that these properties make porous metal foams more attractive in engineering applications such as electro-shielding, blast mitigations, aerospace industry, and in many more applications that are not mentioned here but open to the imagination of engineers and researchers. The future of porous metal foams is bright. It is well evident that the use of state-of-the art metal foams is fast growing. Their utility in several fields of industry such as aerospace, automotive, construction, etc., is driving their demand for mass production.

Technological advancements in recent years have also led to increased production capacity. In comparison to conventional materials, metal foams can be produced at a lesser cost. Development of models will further help in increasing the production rate, properties, quality, and durability. The last but equally crucial aspect is the cost reduction of foam structures which will ensure aggressive quantitative and qualitative growth of the market in future.

Currently, very limited types of materials are explored in their foam counterpart. Aluminum, nickel, cobalt, and steels are the most investigated ones so far. There is an urgent need to exploit more and environment-friendly and stable metals for use as foams. The potential areas of applications are progressively and rapidly emerging due to massive research in this field in finding the appropriate combination of metals or alloys for satisfying the on-field demands of size, shape, density, strength, stiffness, energy absorption, acoustic behaviour, etc. Further, as fuel and energy conservation are extremely sought after to avoid global warming, it is likely more applications will emerge in that direction and hence exploring new materials is very critical at this juncture.

4. CONCLUSION

In conclusion, the research on damping in porous metal foams and its applications has shown great potential. The influence of porosity on damping properties was examined, revealing the intricate relationship between pore size, distribution, and damping behaviour. We uncovered the frequency-dependent nature of damping, a crucial aspect in vibration control applications. The development of metal foams as engineering materials for functional and structural applications is still ongoing. Continued efforts in characterization, modelling, and production techniques will further enhance the understanding and utilization of metal foams in various industries. The versatility of metal foams makes them attractive for a wide range of applications, from structural elements to heat exchangers, energy absorbers, and sound damping elements. With further advancements, metal foams are poised to make significant contributions in the field of materials science and engineering.

REFERENCES

[1] M. F. Ashby, T. Evans, N. A. Fleck, J. W. Hutchinson, H. N. G. Wadley, & L. J. Gibson, Metal foam: s design guide, Elsevier, Oxford, UK (2000).
[2] D. K. Rajak & M.Gupta. An Insight Into Metal Based Foams. Springer, Singapore (2020).
[3] C. Zener, & J. Châtelet, Elasticité et anélasticité des métaux, Edition Dunod, France (1955).
[4] Y. Chevalier, Damping in materials and structures: An overview. Generalized Models and Non-classical Approaches in Complex Materials, Volume 90, 2, 1-27 (2018).
[5] X. Yu, & D. He, Research on the mechanical damping properties of metallic foams'. Mater Mech Eng, 18(3), 26-32 (1994).
[6] J. Banhart, J. Baumeister & M. Weber, Damping properties of aluminium foams. *Materials Science and Engineering: A*, **205**(1-2), 221-228 (1996).
[7] J. N. Wei, C. L.Gong, H. F. Cheng, Z. C. Zhou, Z. B. Li, J. P. Shui, & F. S. Han, Low-frequency damping behavior of foamed commercially pure aluminum. *Materials Science and Engineering*: A, **332**(1-2), 375-381 (2002).
[8] M. oletti, V. Mussi, A. Rossi, & M. Monno, Procedures for damping properties determination in metal foams to improve FEM modeling. *Procedia Materials Science*, 4, 233-238 (2014).
[9] ASTM Standard E756, 2010, " Standard Test Method for Measuring Vibration-Damping Properties of Materials" ASTM International, West Conshohocken, PA, 2010, www.astm.org.
[10] P. Albertelli, S. Esposito, V. Mussi, M. Goletti, & M. Monno, Effect of metal foam on vibration damping and its modelling. *The International Journal of Advanced Manufacturing Technology*, **117**(7-8), 2349-2358 (2021).
[11] L. Dahil, A. Karabulut, & S. Baspinar, Damping properties of open pore aluminum foams produced by vacuum casting and NaCl dissolution process. *Metalurgija*, **52**(4), 489-492 (2013).
[12] Y. Tu, & G. Wang, Damping parameter identification and study of metal foam filled steel tube. *Journal of Materials in Civil Engineering*, **22**(4), 397-402 (2010).
[13] H. Wang, C. Ma, W. Zhang, H. M. Cheng, & Y. Zeng, Improved damping and high strength of graphene-coated nickel hybrid foams. *ACS applied materials & interfaces*, **11**(45), 42690-42696 (2019).
[14] F. García-Moreno, Commercial applications of metal foams: Their properties and production. *Materials*, **9**(2), 85 (2016).
[15] B. FETTAH, Vibration Analysis Of A Shaft Supported By Two Ball Bearings With Metal Foam Damper, PhD dissertation, Hassiba Benbouali University of Chlef, Algeria (2023).
[16] W. Riehemann, A. Finkelstein, U. Arlic, & D. Husnullin, Damping Behavior of Aluminum Replicated Foam. *Progress in Materials Science and Engineering*, 33-40 (2018).
[17] I. S. Golovin, & H. R. Sinning, Damping in some cellular metallic materials. *Journal of alloys and compounds*, **355**(1-2), 2-9 (2003).
[18] J. Banhart, Metal foams-from fundamental research to applications. Frontiers in the Design of Materials, 279 (2007).
[19] J. Banhart, Manufacture, characterisation and application of cellular metals and metal foams. *Progress in materials science*, **46**(6), 559-632 (2001).
[20] G. Srinath, A. Vadiraj, G. Balachandran, S. N. Sahu, & A. A. Gokhale, Characteristics of aluminum metal foam for automotive applications. Transactions of the Indian Institute of Metals, **63**(5), 765–72 (2010).
[21] J. F. RAMÍREZ, M. CARDONA, J. A. VELEZ, et al., Numerical modeling and simulation of uniaxial compression of aluminum foams using FEM and 3D-CT images. Procedia Materials Science, 04, p. 227-231 (2014).
[22] S. RYAN, Shielding against micrometeoroid and orbital debris impact with metallic foams. Orbital Debris Quarterly News, 14(01), 4-7 (2010).
[23] Xiaohu YANG, Junfei GUO, Bo YANG, Haonan Cheng, Pan Wei, Ya-Ling He, Design of non-uniformly distributed annular fins for a shell-and-tube thermal energy storage unit. *Applied Energy*, **279**, 115772 (2020).

NANOMATERIALS
SCIENCE & ENGINEERING
Vol. 7, No. 1, pp. 20-25 (2025)

RESEARCH ARTICLE

https://doi.org/10.34624/nmse.v7i1.37201

The influence of T-Shape flow deflector placement on convection heat transfer over an array heated blocks

AMIRAT Hamza[1, *], KORICHI Abdelkader [1] and AMIRAT Moustapha [2]

[1]University of Yahia Fares, Laboratory of Mechanics, Physics and Mathematical Modeling (LMP2M) Medea, Algeria
[2] Ecole Militaire Polytechnique, Algiers, Algeria

**Corresponding author, e-mail address: amirat.hamza@gmail.com*

Received 30 July November 2024; accepted 15 January 2025; published online 31 January 2025

ABSTRACT

In this research, a numerical study was conducted to examine the convective heat transfer in a horizontal channel containing multiple heated blocks. The channel design incorporates T-shaped flow deflectors strategically positioned downstream of each block. Air, with a Prandtl number of 0.71 and consistent thermal properties, is used for cooling. The geometric attributes and arrangement of the flow deflectors remain consistent throughout the analysis. The computations are based on a Reynolds number of 400, with systematic variations in the positions of the flow deflectors. The finite volume method, implemented using Ansys Fluent© software, is employed to solve the governing mathematical equations numerically. The results emphasize the significant impact of adjustments to the flow deflector configuration on both fluid flow patterns and heat transfer characteristics across the heated blocks.

1. INTRODUCTION

The temperature rise is a significant concern in various engineering disciplines, such as nuclear power, electronics, and mechanical engineering. Higher temperatures can negatively impact the efficiency and lifespan of engineering products. As a result, thermal engineers are compelled to develop and improve innovative strategies to enhance cooling processes. The existing literature is rich in studies addressing this challenge. For example, Bergles et al. [1] outline 13 methodologies to improve heat transfer in industrial settings. Similarly, Yeh [2] provides a concise overview of the cooling techniques commonly used in the electronics industry. A substantial body of research, as cited in [3-8], has focused on heat transfer dynamics across multiple heated blocks. In a specific study, Herman and Kang [9] investigated the effectiveness of curved deflectors in manipulating airflow to displace warm air trapped between blocks, thereby enhancing heat transfer efficiency. While their results showed positive effects on heat transfer, they also noted a corresponding increase in pressure losses, estimating it to be two to three times higher than scenarios without curved deflectors. Additionally, their findings indicated a correlation between improved heat transfer and higher Reynolds numbers. This concept of curved deflectors as a method for enhanced heat transfer, despite the associated increase in pressure loss, was further supported by numerical and experimental investigations conducted by Lorenzini-Gutierrez et al. [10] and Luviano-Ortiz et al. [11]. Based on the insights derived from the preceding literature review, a considerable body of research has focused on enhancing heat transfer over heated blocks through the use of diverse flow deflectors and vortex promoters. In light of this, the current study seeks to explore the influence of varying positions of T-shaped flow deflectors on convective heat transfer across an array of heated blocks.

2. PHYSICAL MODEL AND MATHEMATICAL FORMULATION

2.1. Setups and Description

In this study, Figure 1a depicts the physical model under investigation. The system's geometric layout features two parallel plates (2D) housing five heated blocks. All measurements are unitless, relative to the channel width H. The heated blocks share identical dimensions (w=h=H/4=0.25). Furthermore, distinct flow deflectors are mounted behind each block; their shapes and sizes are detailed in Figure 1b. Each deflector is positioned at h/2 intervals along the longitudinal axis after every block and at a h distance along the transverse axis. The channel's walls are designed as adiabatic surfaces, except for the heated blocks' base, which experiences a uniform heat flux. At the inlet of the channel (u_{inlet}), a forced flow is implemented. The channel is divided into two parts before and after the blocks, with lengths denoted as L_{in}=3 and L_{out}=20, respectively. Due to the significant disparity in the third dimension compared to the others, we simplify the problem by treating it as a two-dimensional (2D) scenario.

Assuming a constant, laminar, and incompressible flow, the fluid's thermophysical properties are constant and it follows Newtonian laws. The corresponding mathematical formulas for the physical model in a non-dimensional format can be organized as follows, assuming that buoyancy and viscous dissipation are ignored:

Mass:

$$\frac{\partial u}{\partial x}+\frac{\partial v}{\partial y}=0 \tag{1}$$

x-momentum:

$$\mathrm{Re}\left(u\frac{\partial u}{\partial x}+v\frac{\partial u}{\partial y}\right)=-\frac{\partial p}{\partial x}+\left(\frac{\partial^2 u}{\partial x^2}+\frac{\partial^2 u}{\partial y^2}\right) \tag{2}$$

y-momentum:

$$\mathrm{Re}\left(u\frac{\partial v}{\partial x}+v\frac{\partial v}{\partial y}\right)=-\frac{\partial p}{\partial y}+\left(\frac{\partial^2 v}{\partial x^2}+\frac{\partial^2 v}{\partial y^2}\right) \tag{3}$$

Energy:
The fluid phase:

$$P_e\left(u\frac{\partial \theta_f}{\partial x}+v\frac{\partial \theta_f}{\partial y}\right)=\left(\frac{\partial^2 \theta_f}{\partial x^2}+\frac{\partial^2 \theta_f}{\partial y^2}\right) \tag{4}$$

The solid phase:

$$\frac{k_{sl}}{k_f}\left(\frac{\partial^2 \theta_{sl}}{\partial x^2}+\frac{\partial^2 \theta_{sl}}{\partial y^2}\right)=0 \tag{5}$$

Non-dimensional variables:

$$x=\frac{x^*}{H^*};\ y=\frac{y^*}{H^*};\ u=\frac{u^*}{u_m^*};\ v=\frac{v^*}{u_m^*};$$
$$\theta=\frac{(T-T_0)}{(q''.H^*/k_f)};\ p=\frac{p^*.H}{\mu_f\,.\,u_m^*} \tag{6}$$

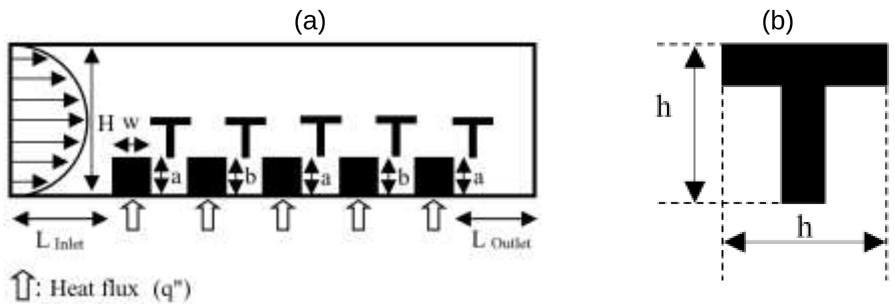

Figure 1. (a): Physical domain channel; (b): Geometric of the **T-shape** deflector.

Table 1. Boundary conditions.

	Border of the geometry	Boundary conditions
Hydrodynamic conditions	Inlet	$\frac{\partial p}{\partial x} = 0;\ U_{inlet} = 6y(1-y);$ $v = 0$
	Outlet	$\frac{\partial u}{\partial x} = \frac{\partial v}{\partial x} = 0;$ The pressure is equal to the ambient pressure
	Channel walls Block bases Solid-Fluid interface	$u = v = 0$
Thermal conditions	Inlet	$\theta_f = 0$
	Outlet Channel walls	$\frac{\partial \theta_f}{\partial x} = 0$
	Block bases	q"= 1
	Solid-Fluid interface	$\theta_f = \theta_{sl};$ $k_f \frac{\partial \theta_f}{\partial n} = k_{sl} \frac{\partial \theta_{sl}}{\partial n}$

And the relevant non-dimensional numbers are:

$$Re = \frac{\rho_f . u_m . H}{\mu_f};\ Pr = \frac{\mu_f . c_{p_f}}{K_f};\ Pe = Re.Pr \qquad (7)$$

2.2. Boundary Conditions

Table 1 provides a condensed compilation detailing the boundary conditions.
Selecting L_{in}=3 and L_{out}=20 arises from an extensive analysis, where calculations delved into diverse scenarios incorporating different inlet and outlet distances.

2.3. Numerical Solution and Validation

The solution of the governing equations within the described physical model is reached numerically utilizing the finite volume approach. Ansys Fluent® serves as the platform for simulation, employing the Simple algorithm. The validation assessments of grid independence and accuracy of computations have been conducted in previous studies [12], using local Nusselt numbers. The results of grid configuration 1,350 × 110 are judged to satisfy Re=400 requirements. Furthermore, close alignment with the research conducted by Young and Vafai is demonstrated, with a maximum deviation of less than 3%. Iterative calculations are conducted until convergence states are achieved. The residuals for every independent parameter are constrained to 10^{-6}.

3. RESULTS AND DISCUSSION

Computational simulations are conducted for flow deflectors with T-shapes at a Reynolds number 400. The outcomes regarding streamlines, temperature profiles, and the mean Nusselt number (derived from equation 9) are presented.

$$Nu_x = \frac{h_c . H^*}{k_f} = -\frac{1}{\theta_s} . \frac{\partial \theta_f}{\partial n} \qquad (8)$$

$$\overline{Nu} = \frac{1}{A} \int_A Nu_s \, ds \qquad (9)$$

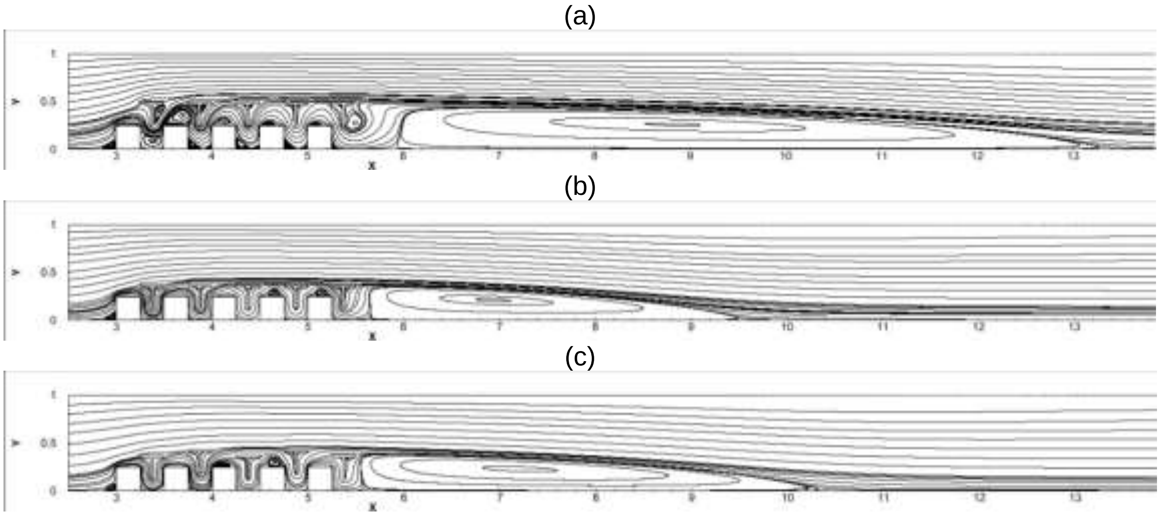

Figure 2. Streamlines for T-shaped deflectors at Re=400, with different deflector positions: (a) a=b=0.25, (b) a=b=0.125, (c) a=0.125; b=0.253.

3.1. Streamlines

In Figure 2, when the distance between the flow deflectors and the bottom of the cavity is decreased to a=b=0.25, also for the flow deflectors position a=0.125 and b=0.25, the flow penetrates more deeply into the gaps between the blocks. Figures 2b and 2c illustrate the case of a=b=0.125, where all vortices between the blocks are completely eliminated. It is evident that the largest vortex, located after the last deflector, decreases in size as the distances a and b decrease to 0.125. This reduction in size causes the vortex to move closer to the last deflector, almost halfway. It is important to note that in the case of a=b=0.25, some of the vortices above the blocks' faces are eliminated, while others are displaced to the right of the blocks' central axes. This change in vortex behavior occurs when the flow deflector positions change to a=b=0.125 (Figures 2b) and a=0.125; b=0.25 (Figures 2c). In the scenario where a=0.25 and b=0.125 (refer to Figure 3.1C), the vortex behind the last block's deflector moves to the left, positioning itself right next to the deflector. Furthermore, it increases in size compared to the case where a=b=0.125 but remains smaller than when a=b=0.25.

It's crucial to understand that reducing the distance between the deflectors and the base of the cavities limits the flow passage section between the blocks and the deflectors. This causes the airflow speed to increase in these areas, improving heat transfer through convection. The same effect occurs when the distance between the last blocks and the vortex after the last deflector is reduced. Thus, it is very important to note that all vortices near the blocks present areas of heat accumulation. The deflectors minimize the mixing of fluid airflow by separating the airflow around the blocks from the airflow above the deflectors. This phenomenon could negatively affect heat transfer through the blocks.

3.2. Isotherms contours

As shown in Figure 3, the temperature of the solid and fluid phases increases as the vertical distance between the deflectors and the bottom of the cavities decreases to a=b=0.125. This leads to isolating the airflow around the blocks from the airflow above the deflectors. This effect is more noticeable in the fourth and fifth blocks due to the increased of heat loaded by the cooling fluid in these regions. Let's consider the case where the positions of the deflectors are a=0.125 and b=0.25, as shown in Figure 3c. These deflector positions allow the airflow to move more freely and improve the mixing and contact of the hot airflow around the blocks with the cooler airflow above the deflectors. This improves the heat transfer between the two airflows, thereby increasing the heat transfer around the blocks compared to the case with the

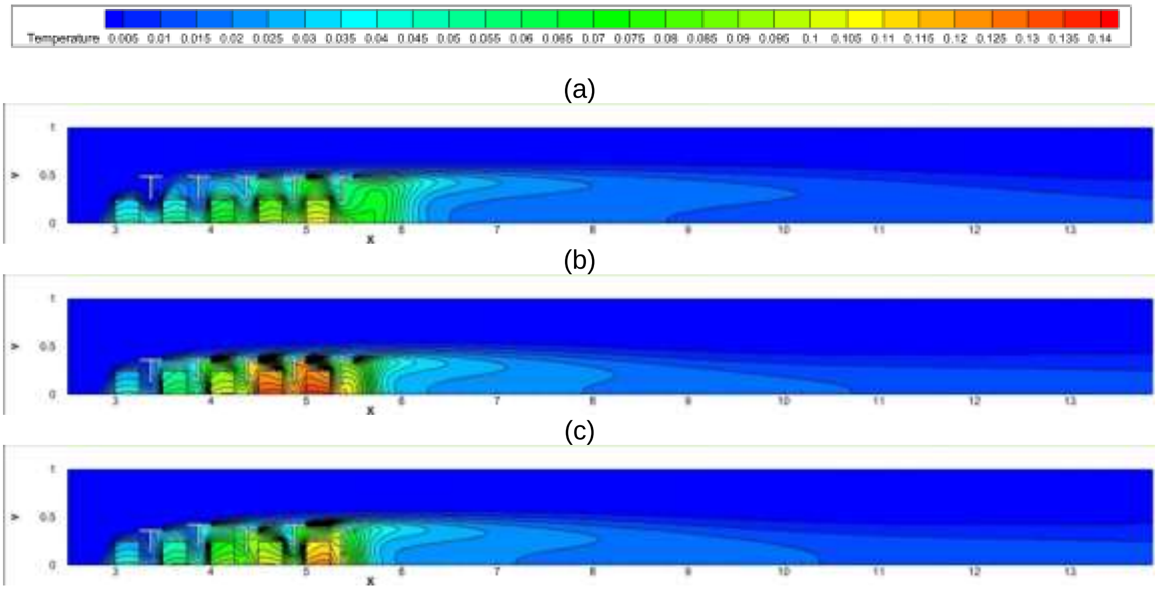

Figure 3. Isotherm contours for T-shaped deflectors at Re=400, with different deflector positions: (a) a=b=0.25, (b) a=b=0.125, (c) a=0.125; b=0.25.

deflectors positioned at a=b=0.125. The best position for optimal cooling is the case where a=b=0.25, followed by the position a=0.125 and b=0.25. The worst cooling condition corresponds to the position a=b=0.125. It is important to note that the positions of the deflectors influence the shape of the temperature contours inside and outside the heated blocks.

3.3. Mean Nusselt Number

Heat transfer is countified using the mean Nusselt number, presented in Figure 4. The position of T-

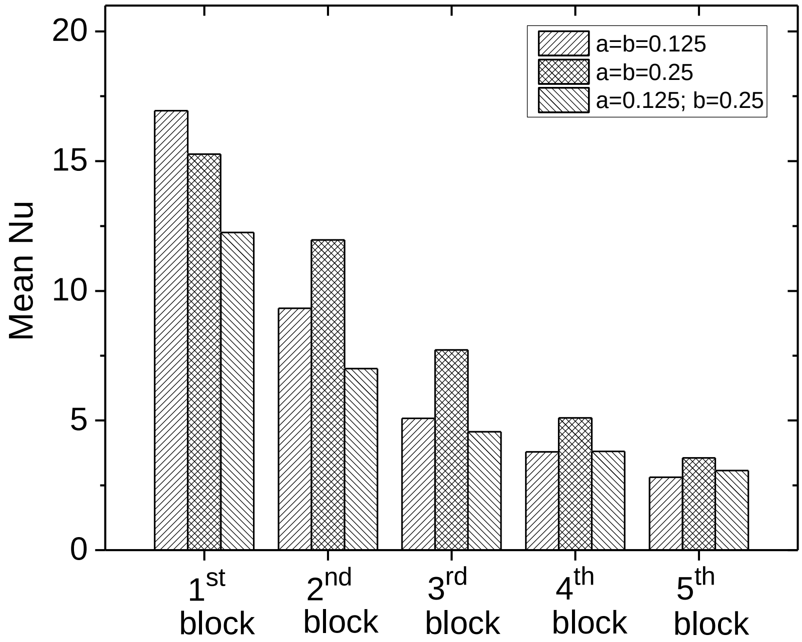

Figure 4 The average Nusselt numbers for the cases with and without T-shaped deflectors.

shaped deflectors has a considerable effect on heat transfer. For the first block, position a=b=0.125 gives the best heat transfer, followed by position a=b=0.025, and then the case with position a=0.125 and b=0.25. Regarding the other blocks, the highest heat transfer is observed with the deflectors at position a=b=0.25, followed by the deflectors at position a=b=0.125, except for the fourth block, which shows that the heat transfer for the deflectors at positions a=b=0.125 and a=0.125, b=0.25 is approximately the same. The same applies to the last block but with finer variations. The change in heat transfer behavior with different deflector positions between the first block and the others occurs because the cooling air around the blocks experiences a temperature increase due to low mixing and separation provided by the deflectors.

4. CONCLUSION

The study used numerical simulations to analyze fluid flow and forced heat transfer over heated blocks with T-shaped flow deflectors. It aimed to investigate the influence of the deflectors' position at a Reynolds number of Re=400. The simulations examined three positions of the flow deflectors and highlighted the significant impact of the deflectors' position on flow and thermal fields.

The deflectors effectively eliminate vortices in the space between the blocks, especially when properly shaped and positioned. Vortices typically form on the upper faces of the heated blocks. Moreover, the vortex following the last deflector is directed away from the rear face of the last block. Eliminating vortices near the blocks could potentially enhance heat transfer around the blocks through improved convection in these regions. The presence of deflectors diminishes the flow mixing, consequently impairing heat transfer efficiency in the terminal three blocks. Such reduction in flow mixing attenuates the enhancement in heat transfer that could be achieved through the augmented thermal energy transported by the fluid. The most unfavorable position for cooling the blocks is a=b=0.125. The results are clearer for the fourth and fifth blocks. The most effective cooling configuration is attained when the values of both variables a and b are precisely set to 0.25. For the initial block, optimal thermal efficiency, indicated by the highest mean Nusselt number, occurs at a=b=0.125. Conversely, suboptimal thermal performance is observed at a=b=0.25. Subsequent evaluations reveal that a configuration of a=b=0.25 emerges as the preferable setup, optimizing thermal efficiency across the remaining blocks.

REFERENCES

[1] A.E. Bergles, V. Nirrnalan, G.H. Junkhan, and R.L. Webb, Bibliography on augmentation of convective heat and mass transfer II, Heat Transfer Laboratory Report HTL-31, ISU-ERI-Ames- 84221, Iowa State University, Ames (1983).

[2] L. Yeh, J. Electron. *Packag.* **117**, 333–339 (1995).

[3] J. Young, and K. Vafai, *J. Heat Transfer*, **12**, 34–42 (1999).

[4] T. J. Young, and K. Vafai, *Int. J. Heat Mass Transf.*, **41**, 3279–3298 (1998).

[5] J. S. Nigen, and C. H. Amon, *J. Fluids Eng.*, **116**, 499–507 (1994).

[6] G. Imani, M. Maerefat, and K. Hooman, *Numeri. Heat Transf. A Appl.*, **62**, 798–821 (2012).

[7] J. Davalath, and Y. Bayazitoglu, *J. Heat Transfer*, **109**, 321–328 (1987).

[8] F. P. Incropera, *J. Heat Transfer*, **110**, 1097–1111 (1988).

[9] C. Herman, and E. Kang, *Int. J. Heat Mass Transf.*, ***45**, 3741–3757 (2002).*

[10] D. Lorenzini-Gutierrez, A. Hernandez-Guerrero, J. L. Luviano-Ortiz, and J. C. Leon-Conejo, *Appl. Therm. Eng.*, **75**, 800–808 (2015).

[11] L. Luviano-Ortiz, A. Hernandez-Guerrero, C. RubioArana, and R. Romero-Mendez, *Int. J. Heat Mass Transf.*, **51**, 972–3984 (2008).

[12] H. Amirat, and A. Korichi, *Journal of Mechanics*, **36**, 19-131 (2020).

Nanomaterials Science & Engineering (NMS&E), Vol.7, No.1, 2025

Department of Mechanical Engineering
University of Aveiro
Aveiro 3810-193
Portugal

https://proa.ua.pt/index.php/nmse/

ISSN: 2184-7002

university of aveiro tema centre for mechanical technology and automation